Does High-Entropy Oxide $(CrMnFeCoNi)_3O_4$ Catalyst Require Support to Improve Performance in CO_2 Hydrogenation?

Ksenia A. Kokina [a], Anton S. Konopatsky [a,b,*], Ekaterina S. Chikanova [a], Danil V. Barilyuk [a], Tatyana O. Teplakova [a], Denis V. Leybo [c], Ekaterina V. Sukhanova [d,e], Zakhar I. Popov [d], Alexey Y. Antonov [f], Olga A. Boeva [f], Sergey A. Efimov [f], Dmitry V. Shtansky [a]

[a] *National University of Science and Technology "MISIS", Leninsky prospect 4, Moscow 119049, Russia*
[b] *Normandie Univ., ENSICAEN, UNICAEN, Caen 14000, France*
[c] *Schulich Faculty of Chemistry, and Resnick Sustainability Center for Catalysis, Technion, Israel Institute of Technology, Technion City, Haifa 32000, Israel*
[d] *Emanuel Institute of Biochemical Physics RAS, Kosygina 4, Moscow 119334, Russia*
[e] *Moscow Institute of Physics and Technology, Institutsky lane 9, Dolgoprudny, Moscow 141700, Russia*
[f] *Mendeleev University of Chemical Technology of Russia, Moscow, Russiag Skolkovo Institute of Science and Technology, Skolkovo Innovation Center, Moscow 143026, Russia*

h National Research Nuclear University MEPhI, Kashirskoe Shosse 31, Moscow 115409, Russia

i Institute of Solid State Physics RAS, Chernogolovka, Moscow Region 142432, Russia

**E-mail address:* konopatskiy@misis.ru (Anton S. Konopatsky)

STEM images of the HEO/TiO_2 and HEO/BN samples are collected in Figure S1.

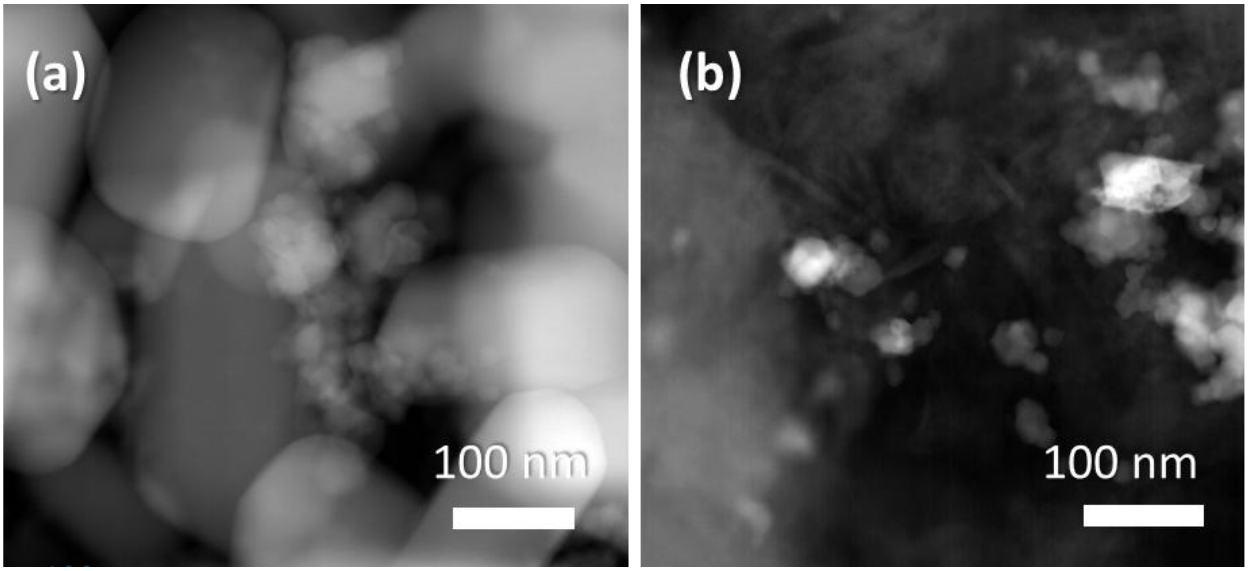

Fig. S1. STEM images of HEO/TiO_2 (a) and HEO/BN (b) materials.

The results of EDX spectroscopy analysis performed for all the samples studied are given in Table S1.

Table S1. Material elemental composition as determined by EDX spectroscopy

Sample	Chemical composition, at.%								
	Cr	Fe	Co	Ni	Mn	O	B	N	Ti
HEO	9.6	9.3	9.4	5.6	8.1	57.9	-	-	-
HEO/BN	1.0	0.9	0.8	0.4	0.7	19.7	45.4	31.1	-
HEO/TiO_2	0.3	0.3	0.3	0.2	0.2	74.0	-	-	24.7

EDX spectra of HEO (a), HEO/BN (b) and HEO/TiO_2 are collected in Figure S2.

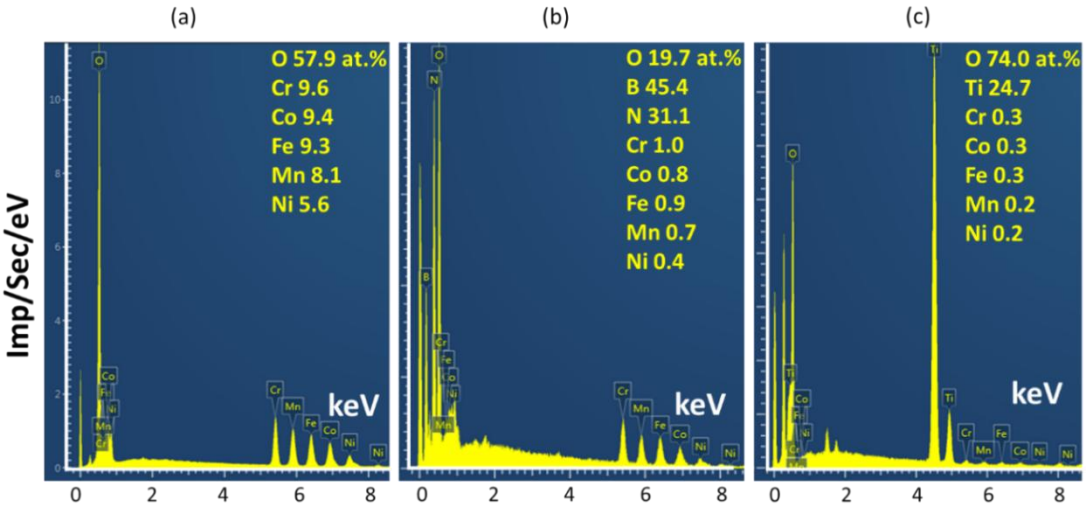

Fig. S2. EDX spectra of HEO (a), HEO/BN (b) and HEO/TiO_2 (c) samples.

DTGA curves allow us to investigate mass loss rate of all samples at higher temperature (Figure S3). The reduction process is most pronounced in the curve of the freestanding HEO NPs. For the curves corresponding to the supported samples, the mass loss is less pronounced but still noticeable compared to the carrier curves. It should be noted that the aliquots of the supported samples contained 4.3 mg of HEO, whereas the bare HEO sample weighed 34.7 mg, eight times more. No mass loss was observed for the pure carrier samples in this temperature range.

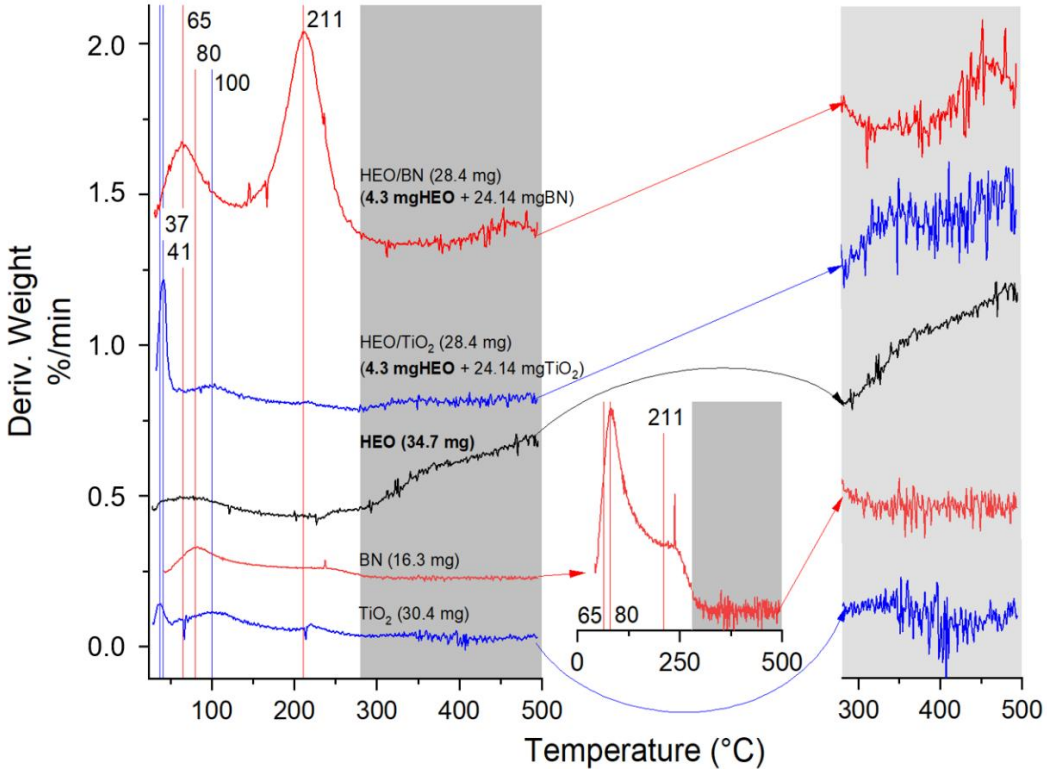

Fig. S3. DTGA curves analysis for all studied materials.

Table S2 compares HEO NPs with other catalytic materials in the CO_2 conversion reaction. However, it is worth noting that the reaction conditions differ both in terms of pressure values, which largely determine the reaction mechanism and material selectivity, and in the H_2/CO_2 ratio, which significantly affects the conversion value. The HEO NPs show an exceptionally high CO_2 conversion at $H_2/CO_2 = 2$. This is especially noticeable when compared to other multicomponent systems with comparable or lower conversion at higher H_2/CO_2 ratio. The H_2/CO_2 ratio of 2 is not stoichiometric, which leads to hydrogen deficiency. Therefore, the conversion values of 46% is in fact close to the highest possible conversion in the given conditions.

Table S2. Comparison of different catalysts in the CO_2 hydrogenation/methanation reactions

Catalyst	T_{act}, °C	H_2/CO_2	P, MPa	T, °C	X (CO_2), %	VHSV, $L*g_{cat}^{-1}*h^{-1}$	Ref
$(CrFeCoNiMn)_3O_4$	500	2	2	380	46	10.88	This work
$Fe_xNi_2CrCoMnO_y$	600	4	0.1	400	73	9	[1]
Fe-Co/K-Al_2O_3	400	3	2	320	49	3	[2]
$Co_3MnNiCuZnO_x$	600	3	0.1	500	47	20	[3]
10Ni/Ce-ZrO_2	450	4	0.1	275	55	20	[4]
10% Ni/TiO_2	400	4	0.1	350	53.5	60	[5]
0.03% Pt-20% Co-80% Al_2O_3	400	4	0.1	400	70	36	[6]
Ni/CaO-Al_2O_3	450	4	0.1	400	81	48	[7]
CuO-ZnO-TiO_2-ZrO_2	300	3	3	240	43.8	2.4	[8]
Fe-K/γ- Al_2O_3	450	3	1	300	30.9	1.8	[9]
Fe-Cu-K-Al	450	3	0.1	300	39.4	2	[10]
5Mn-Na/Fe	350	3	3	320	38.6	2.04	[11]
$La_{0.9}Sr_{0.1}CuO$	300	2.85	3	300	9.18	8.6	[12]
10Mn-Fe3O4	400	3	2	350	44.7	4	[13]
5% Pt/(NiMgCuZnCo)O	500	3.3	0.1	500	47.8	8.66	[14]

The crystal structure and phase composition of all samples subjected to the activation were studied by XRD. The samples were activated, cooled to room temperature and then transferred to the XRD setup. Note that this leads to an inevitable passivation of the reduced samples. The changes in the phase composition are clearly visible for the freestanding HEO NPs (Figure S4a), less noticeable for the HEO/BN sample (Figure S4b) and indistinguishable for HEO/TiO_2 material (Figure S5) due to the low content of the active phase and the overlap of the HEO/substrate reflections. However, after 400 °C activation, no noticeable changes in the HEO phase composition were observed. The possibility that no reduction occurred at this temperature can be ruled out since the same catalytic efficiency was observed for the HEO samples. It can therefore be assumed that some HEO was reduced to the metallic state and then passivated in air. However, in the case of HEO NPs activated at 500 °C, a set of (111), (200) and (220) peaks of a multicomponent alloy are observed. Apparently, most of the HEO was reduced and air passivation did not lead to complete oxidation. The XRD patterns of HEO NPs activated at 600 °C and 500 °C are similar.

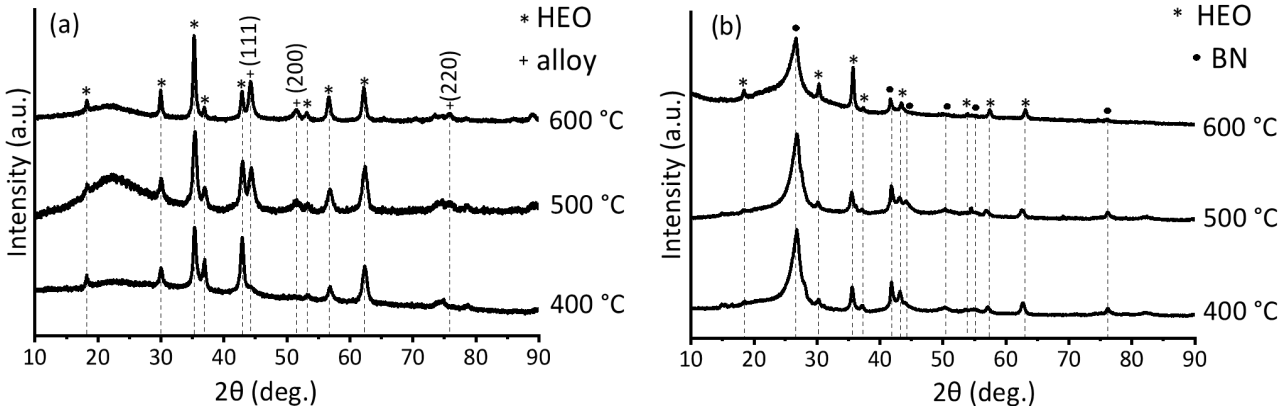

Fig. S4. XRD patterns of HEO (a) and HEO/BN (b) samples after activation at 400°C, 500°C and 600°C.

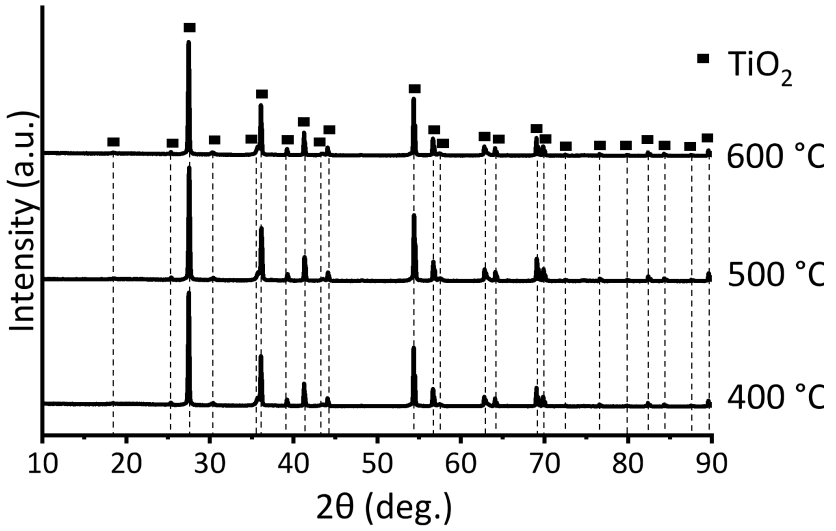

Fig. S5. XRD patterns of HEO/TiO_2 samples after activation at 400°C, 500°C and 600°C.

The X-ray diffraction results for catalysts after conversion tests are shown in Figure S6.

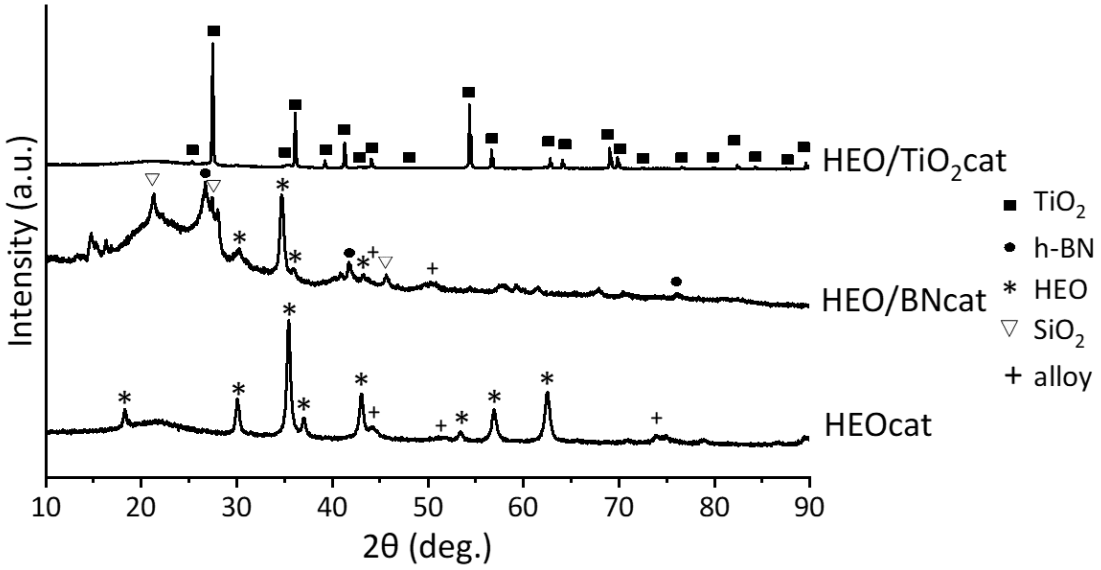

Fig. S6. XRD patterns of HEO, HEO/BN and HEO/TiO_2 samples after catalysis

A comparison of the reaction rate of HEO NPs with some other catalysts is given in Table S3.

Table S3. Reaction rates of various catalysts in CO_2 hydrogenation reaction

Catalyst	T, °C	CO_2 activity μmol/g*s	Ref
$(CrFeCoNiMn)_3O_4$	380	6.68	This work
$NiO/ZnAl_2O_4$	450	10.6	[15]
$0.08wt\%Na/ZnFe_2O_4$	340	1.807	[16]
Co_3O_4	450	3.335	[17]
$Cu_xZn_{1x}Al_2O_4$	250	0.687	[18]
3.5 wt% Rh/TiO_2	500	13.6	[19]
$Co_3MnNiCuZnO_x$	500	0.003	[3]
5% Pt/(NiMgCuZnCo)O	500	0.012	[14]
ZnFeOx-nNa	320	8.827	[20]

Note the observed systematic shift of the (311) HEO XRD peak towards lower 2θ values, both in the case of activated samples and after their catalytic stability tests (Figure S7), which reaches 0.5–0.7° 2θ for the HEO NPs. In the case of the HEO/BN material, the shift is only 0.3 – 0.4° 2θ. It can be assumed that this shift is associated with the lattice deformation arising from the reduction/oxidation cycles and the corresponding alloy and oxide formation. This shift can be used as a measure of the reduction completeness, which is higher for HEO NPs and lower for HEO/h-BN counterparts. This is another indication that h-BN hinders the HEO reduction.

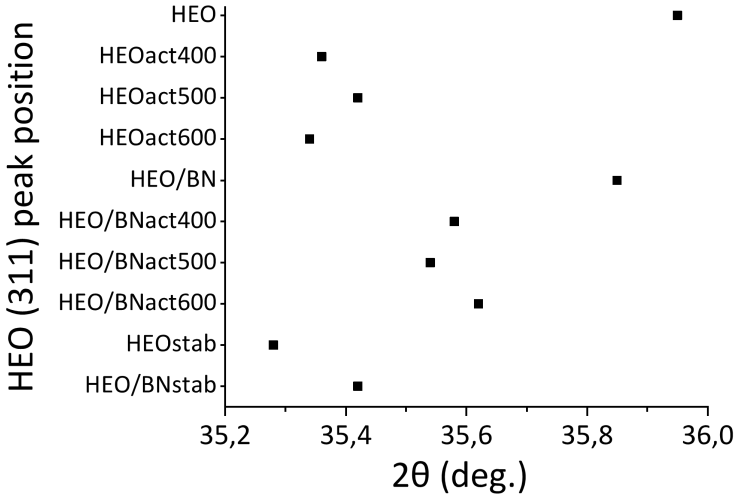

Fig. S7. XRD (311) peak position (2θ) of HEO sample.

The XPS method was used to analyze the surface chemical states of the studied materials. Symmetric peak shapes, typically Voigt profiles, are employed for insulating compounds like most metal oxides. This is because the absence of accessible electronic states at the Fermi level prevents low-energy electron-hole pair excitations, resulting in a symmetrical line shape. Conversely, asymmetric line shapes are necessary for metallic species and certain conducting oxides, where the high density of states at the Fermi level enables screening of the core hole via these excitations, producing a characteristic tail on the high-binding-energy side of the peak [21].

Based on the well-pronounced satellite structure, it is deduced that Co is present as Co^{2+} [22,23]. Please note that despite being represented by a single oxidation state, the main Co 2p peak is approximated by two components. This is due to the final state relaxation effect, which results in two distinct final states upon photoemission. After conversion testing (Figure S8) a peak at 778.4 eV appears, corresponding to metallic Co [24]. Similarly, Ni is also represented as Ni^{2+} ions [22,23,25]. Cr is in the Cr^{3+} oxidation state and is approximated by a multiplet, as

suggested elsewhere [23]. Based on these findings, the following conclusions can be drawn. According to crystal field theory, Cr^{3+} ions are expected to preferentially occupy octahedral sites [26] due to their high crystal field stabilization energy (CFSE). In the HEO sample after conversion testing, a noticeable shift towards lower BE values is observed (Figure S8). The Cr2p 3/2 and Cr2p 1/2 maxima are located at 576.37 eV and 586.0 eV, respectively. The Cr2p 3/2 maximum reveals a new contribution at 575.7 eV, which can be assigned to Cr^{3+} in $Cr(OH)_3$ [27].

Similarly, both Ni^{2+} and Co^{2+} also exhibit high CFSE, suggesting their preference for octahedral coordination, analogous to the cation distribution in an inverse spinel. Therefore, the obtained spinel is neither purely normal nor purely inverse but possesses a complex cation distribution [28].

In the as-synthesized HEO sample, the XPS Mn2p spectrum shows a characteristic doublet at positions 641.6 (Mn2p 3/2) and 653.2 eV (Mn2p 1/2) [29] , which were deconvoluted using three components. The peak at 640.65 eV and a distinct satellite at 645.4 eV indicate the presence of Mn^{2+} species [30], and the maximum at 642.4 eV can be attributed to Mn^{3+} [31]. After conversion testing (Figure S8) an additional component appears at 639.0 eV, which corresponds well to the Mn^0 state [32].

The XPS Fe2p spectrum of the HEO sample was fitted with two components, revealing the presence of Fe^{2+} (710.2 eV) and Fe^{3+} (713.1), which is typical for spinel oxide [33]. In the sample after conversion, the positions of the doublet peaks remain almost unchanged. An additional small maximum at 707.9 eV, observed after spectrum deconvolution, is characteristic of the metallic state of iron [34].

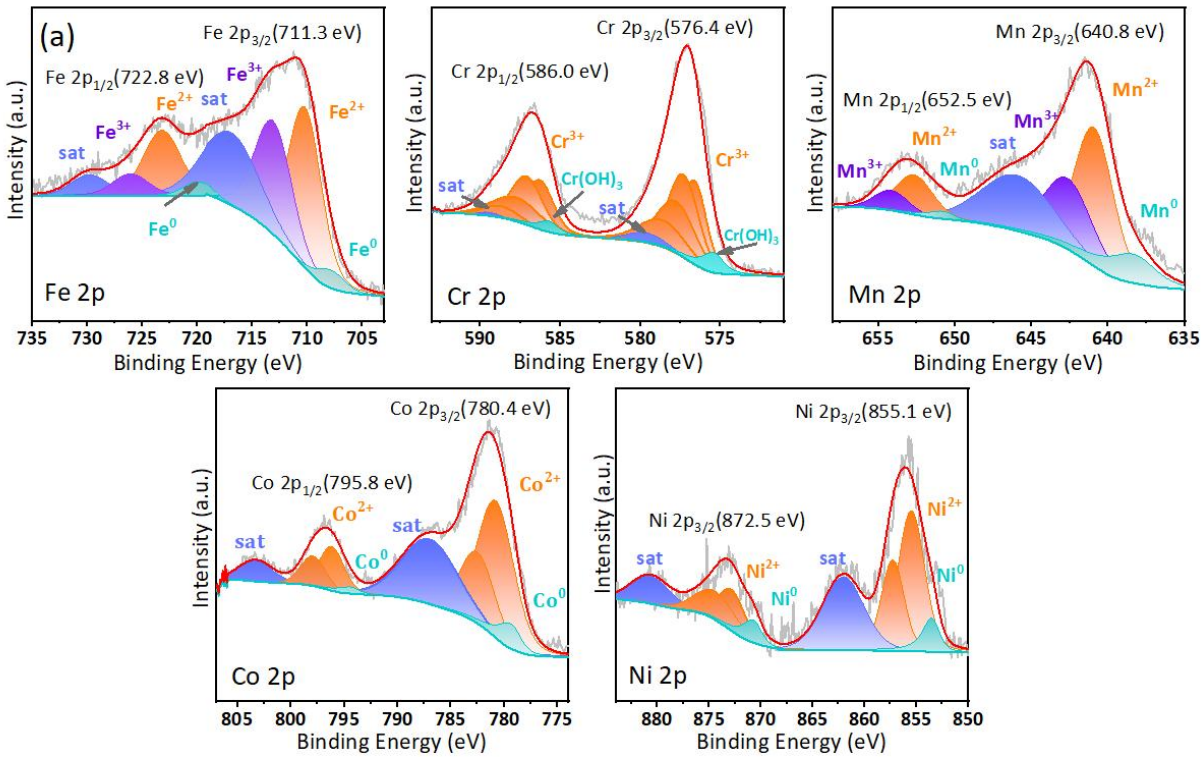

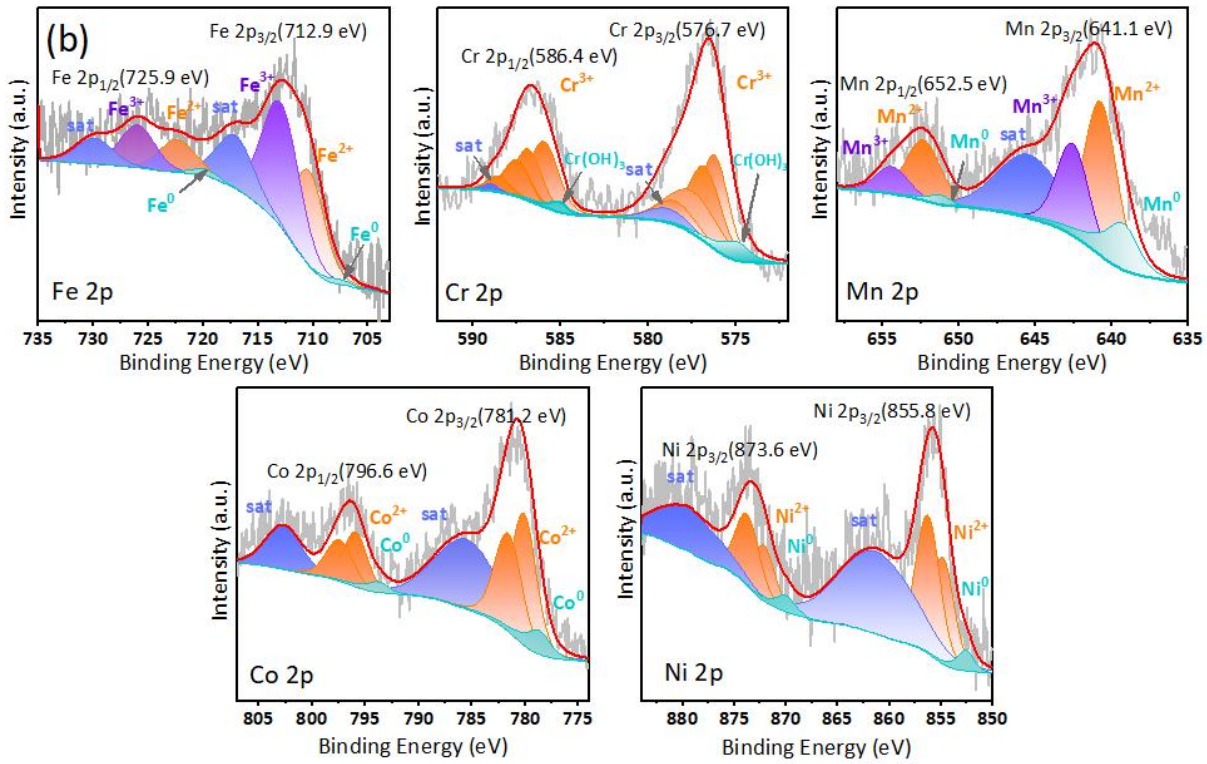

Fig. S8. XPS spectra of HEO materials after conversion (a) and stability (b) tests.

The XPS spectra for supported HEO/TiO_2 and HEO/h-BN samples after stability testing are shown in Figures 9 and 10.

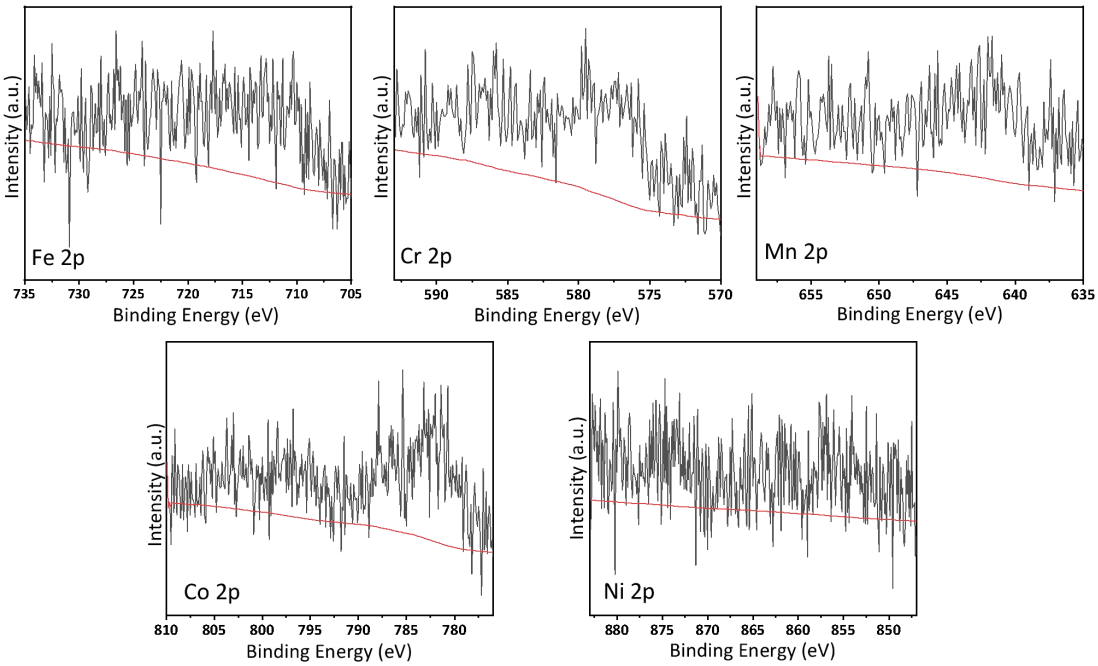

Fig. S9. XPS spectra of HEO/TiO_2 material after stability test.

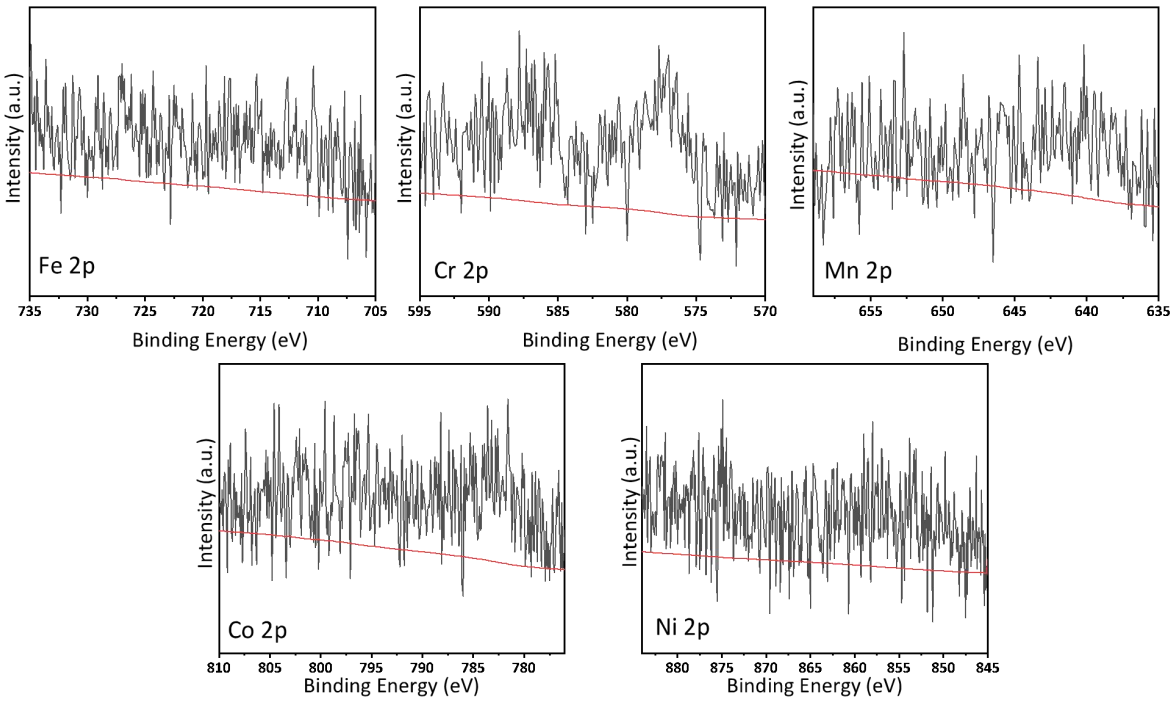

Fig. S10. XPS spectra of HEO/BN material after stability test.

Table S4 presents HEO NP surface composition in as-synthesized state and after catalytic conversion and stability tests.

Table S4. HEO NP surface composition in as-synthesized state and after catalytic conversion and stability tests.

Sample	Concentration, at.%				
	Cr	Co	Fe	Mn	Ni
HEO NPs as-synthesized	24.4	26.6	24.8	22	2.2
HEO NPs after conversion testing	26.7	30	28.3	12	3
HEO NPs after stability testing	33.8	23.7	12	17.5	13

The X-ray diffraction results for catalysts after stability tests are shown in Figure S11.

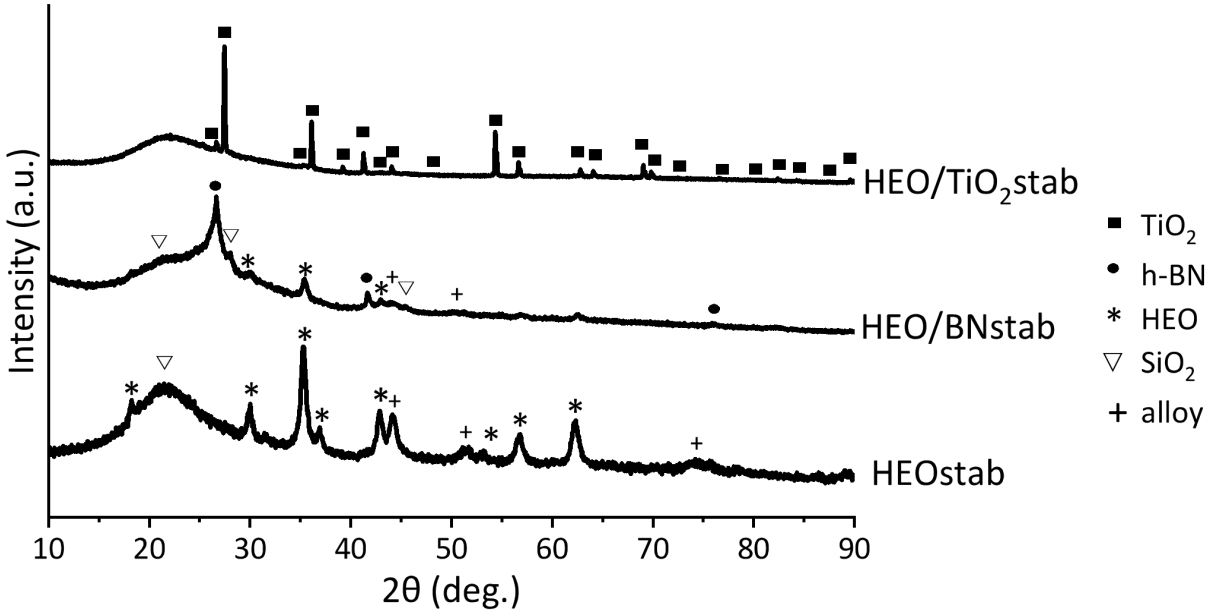

Fig. S11. XRD patterns of HEO, HEO/BN and HEO/TiO_2 samples after stability tests.

STEM images and EDX spectroscopy elemental maps of HEO/BN and HEO/TiO_2 materials after catalytic stability tests are shown in Figures S12 – 14.

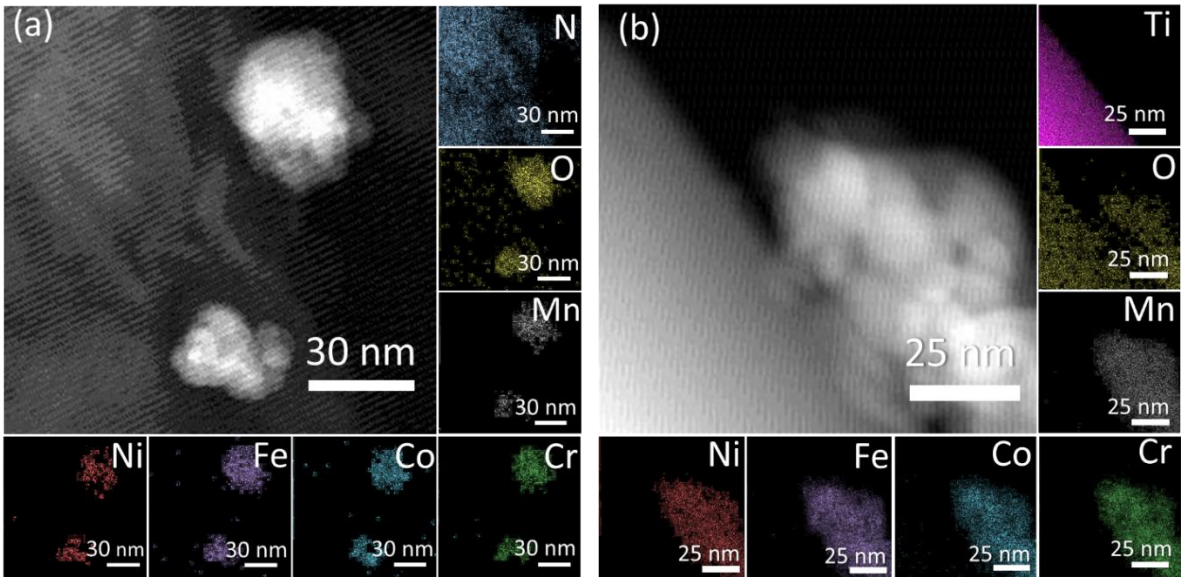

Fig. S12. STEM image and corresponding EDX spectroscopy elemental maps of HEO/BN (a) and HEO/TiO_2 (b) materials after catalytic stability tests. The distribution of boron (B) in the HEO/BN sample is the same as the distribution of nitrogen (N) and is not shown here.

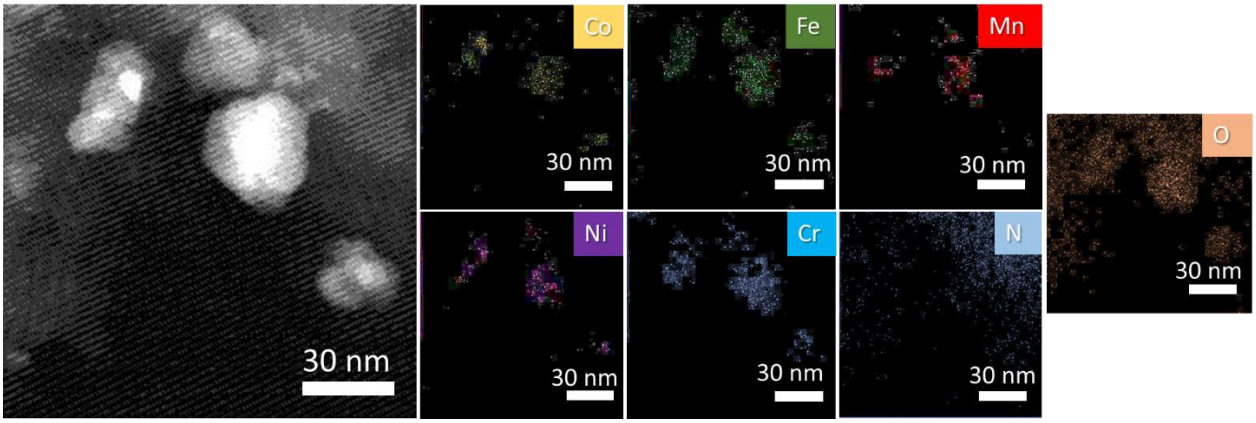

Fig. S13. STEM image and corresponding EDX spectroscopy elemental maps of HEO/BN after catalytic stability tests. The distribution of boron (B) in the HEO/BN sample is similar to that of nitrogen (N) and is not shown here.

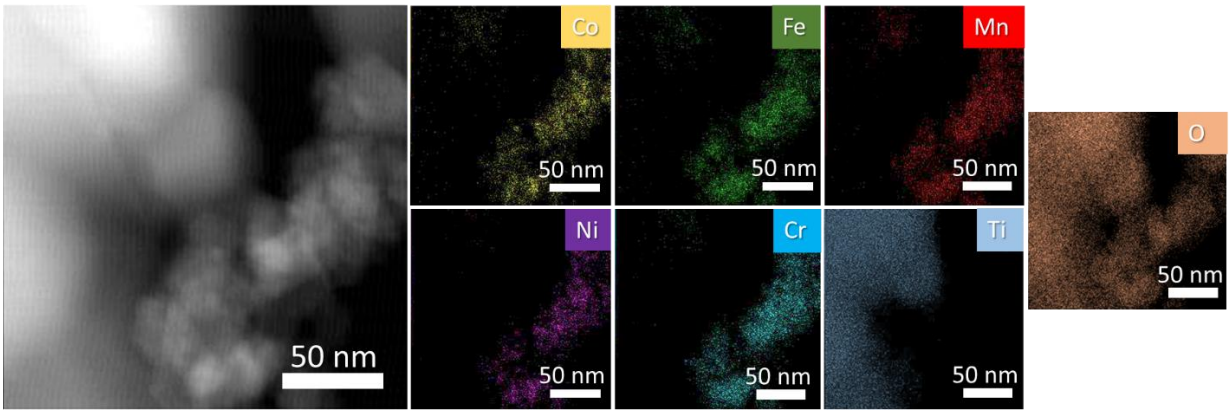

Fig. S14. STEM image and corresponding EDX spectroscopy elemental maps of HEO/TiO_2 materials after catalytic stability tests.

Consequent TPR/TPO profiles is shown in Figure S15.

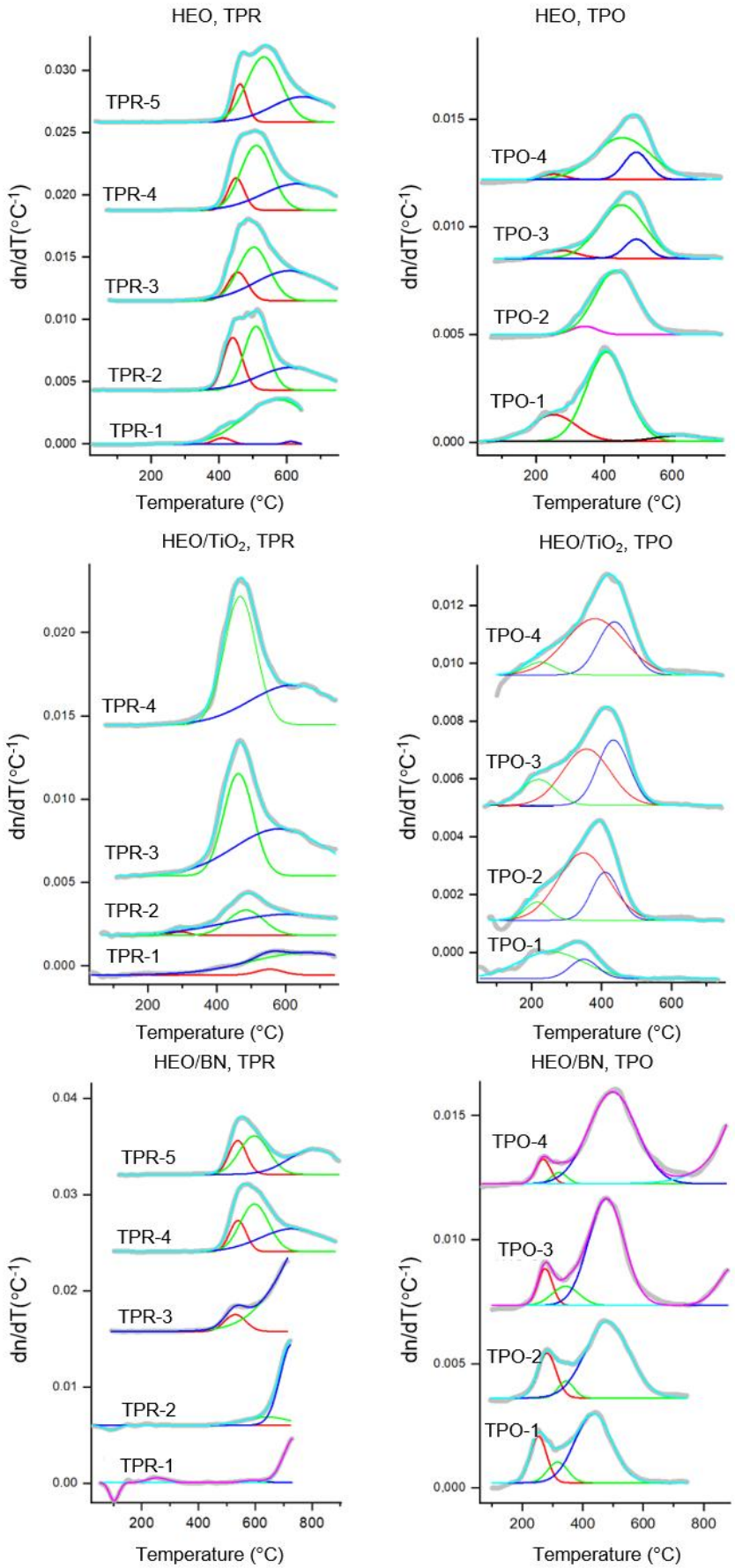

Fig. S15. Consequent TPR/TPO runs.

Comparison of initial TPR curves obtained during first runs are given in Figure S16. For all samples, negative TPR and TGA peaks are observed in the low-temperature region, supporting the hypothesis of water release. TPR and TGA peaks in the 200–300 °C range indicate hydrogen uptake during the reduction of BNO bonds. In TGA profiles, the reduction of HEO is weakly pronounced, whereas in TPR profiles, this process remains clearly detectable up to 650–750 °C. The observed shift of TPR peaks to higher temperatures (by approximately 30 °C) compared to corresponding TGA peaks is attributed to differences in experimental conditions.

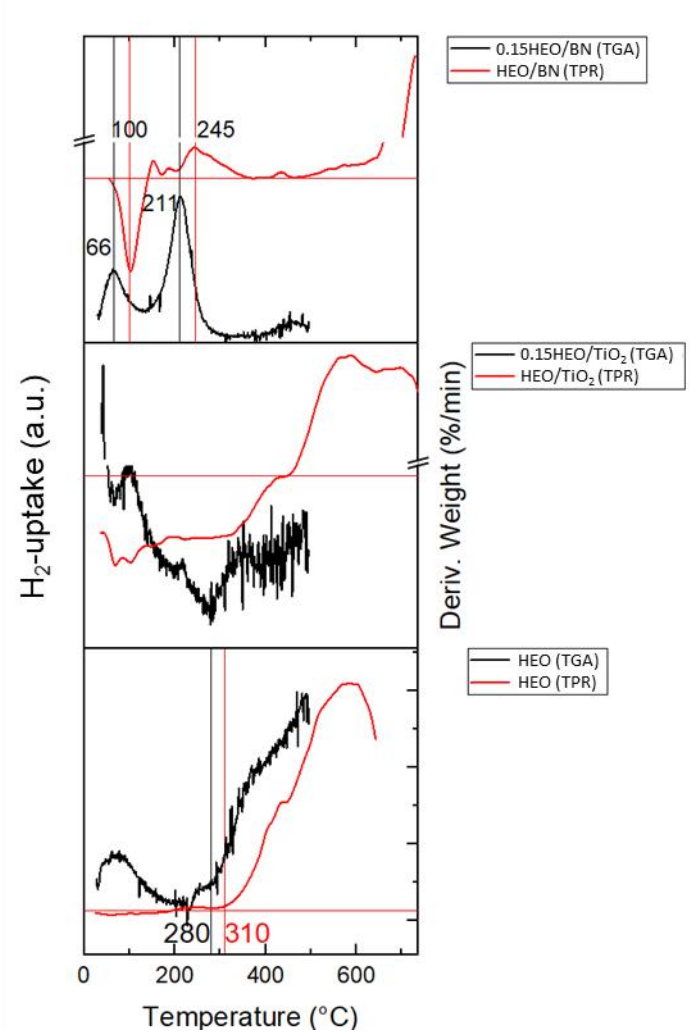

Fig. S16. Comparison of TRP and TGA curves.

Figure S17 collects different H_2/O_2 ratios for HEO NPs, HEO/TiO_2 and HEO/BN samples after consequent TPR/TPO runs. For the HEO and HEO/TiO_2 samples, the H_2/O_2 ratio approaches 2 (corresponding to water formation stoichiometry) starting from the 2nd or 3rd cycle. This indicates the reversibility of the redox processes, which we interpret as reversible transitions between HEO and HEA. In the case of the HEO/BN sample, the H_2/O_2 ratio increases with each subsequent cycle but does not reach 2 within 4 cycles. This suggests an irreversible oxidation process, that could be associated with a constant hydrogen depletion due to adsorption by h-BN. An increase in the maximum temperature, starting from the third oxidation cycle, leads to the following effects: (i) the emergence of an oxygen uptake region above 750 °C; (ii) a decrease in the onset temperature of hydrogen absorption to approximately 450 °C, while the profile shape approaches that characteristic of the HEO and HEO/TiO_2 samples; (iii) a more

rapid increase in the H_2/O_2 ratio. It can be assumed that at a higher temperature and a greater number of TPR/TPO runs, h-BN is saturated with hydrogen and the reduction of HEO NPs becomes more pronounced.

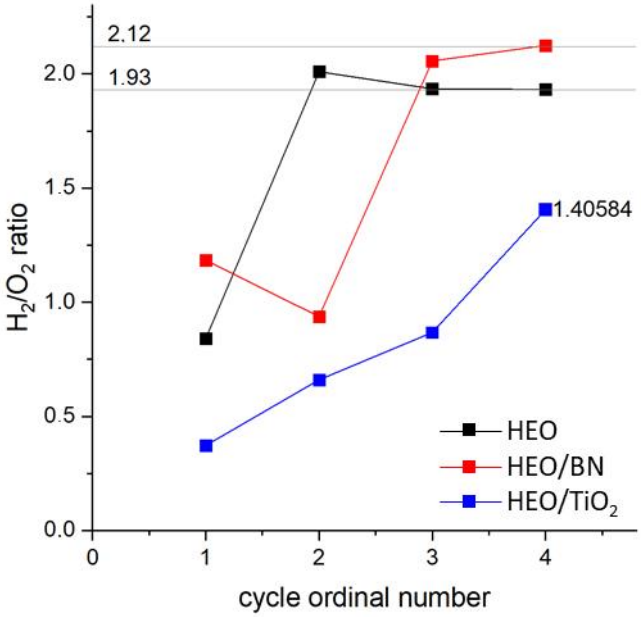

Fig. S17. H_2/O_2 ratios for HEO NPs, HEO/TiO_2 and HEO/BN samples during consequent TPR/TPO runs.

A direct comparison of the TPR profiles of the HEO sample with literature data was performed (Figure S18). The HEO sample was selected for this comparison to eliminate possible influence of HEO-support interactions on the profile shape. When selecting literature data, special attention was paid to studies that present TPR spectra for unsupported oxides. The list of references is presented in Table S5.

The vertical lines in Figure S18 indicate the peak maximum positions in the TPR profiles. The color of each vertical line corresponds to the color of the reference number. Before analyzing the data, it should be noted that oxide reduction typically occurs in several steps ($Me^{n+} \rightarrow Me^{m+} \rightarrow Me^{k+} \rightarrow$..., where $n > m > k$, $k \geq 0$), with each reduction step producing a characteristic peak in the TPR profile, although these peaks are not necessarily fully resolved.

Comparison of the experimental data with literature sources does not reveal absorption in the regions characteristic of chromium[35,36] and nickel[37,38] oxides, as well as in the regions corresponding to higher oxidation states of cobalt, iron, and manganese [39–52]. Thus, a complete absence of absorption is observed in the regions typical for two of the five HEO metals, as well as in the regions characteristic of high oxidation states of the remaining three metals. This additionally confirms both the absence of separate individual oxide phases and the formation of HEO with properties that differ from the sum of the properties of its constituent oxides.

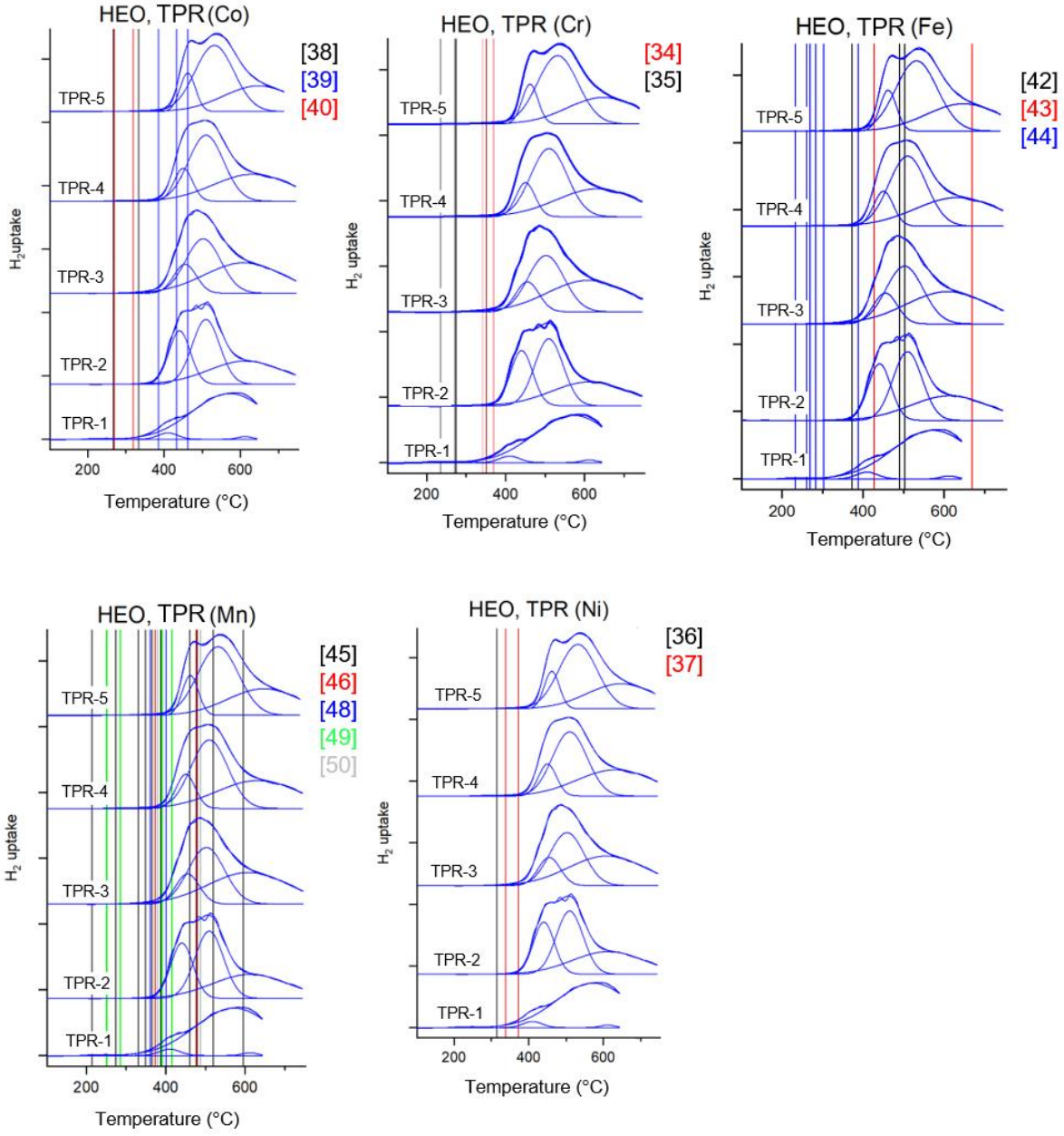

Fig. S18. Comparison of the obtained TPR profiles of HEO NPs with typical TPR peak positions of Co, Cr, Fe, Mn and Ni oxides according to literature data.

Typical TPR peak positions of Co, Cr, Fe, Mn and Ni oxides according to literature data are given in Table S5.

Table S5. Typical TPR peak positions of Co, Cr, Fe, Mn and Ni oxides according to literature data.

No	metal	oxide	support	Tm, ºC	comments	Ref.
1.	Co	Co_3O_4	-	268		[39]
				334		
2.	Co	Co_2O_3	-	386		[40]
				433		
				462		
3.	Co	Co_3O_4	-	270		[41]
				320		
4.	Cr	no data	ZrO_2	350	(%Cr = 0,5)	[36]
				342	(%Cr = 1,0)	
				369	(%Cr = 4,0)	
				350	(%Cr = 8,0)	
5.	Cr	no data	-	234	(Cr^{6+}→….)	[35]
				273		
				274		
				234		
				271		
					(Cr^{n+}→…, n<6)	
				352		
6.	Cr	no data	-	268	(Cr^{6+}→….)	[42]
				348	(Cr^{3+}→….)	
7.	Fe	Fe_2O_3	-	373		[43]
				491		
		Fe_3O_4		503		
8.	Fe	no data	-	428		[44]
				669		
9.	Fe	no data	-	234		[45]
				270		
				262		
				284		
				389		
10.	Mn	MnO_2	-	274		[46]
				331	for various allotropic	
				214	modifications of MnO_2	
				349		
				461		
				596		
				388		
				366		
				479		
				521		
11.	Mn	Mn_2O_3	-	374		[47]
				477		
12.	Mn	Mn_2O_3	-	323		[48]
				417		
13.	Mn		-	550		[41]
14.	Mn	MnO_2	-	361		[49]

				401		
15.	Mn	MnO_2	-	251 283 285 390 291 303 415 317 337	for various allotropic modifications of MnO_2	[50]
16.	Mn	Mn_2O_3	-	379 a 434 a 420 b 487 b 408 c 474 c	letters refer to different possible morphologies	[51]
17.	Mn	MnO_x	-	190 ºC 328 ºC 424 ºC 389 ºC 451 ºC	$MnO_2 \rightarrow Mn_2O_3 \rightarrow Mn_3O_4 \rightarrow MnO$	[52]
18.	Ni	NiO	-	315		[38]
19.	Ni	NiO	-	339 373		[37]

References

[1] Liao Y, He Y, Cui X, Liu L. Elemental Fe conditioning for the synthesis of highly selective and stable high entropy catalysts for CO2 methanation. Fuel 2024;355:129494. https://doi.org/10.1016/j.fuel.2023.129494.

[2] Numpilai T, Witoon T, Chanlek N, Limphirat W, Bonura G, Chareonpanich M, Limtrakul J. Structure–activity relationships of Fe-Co/K-Al2O3 catalysts calcined at different temperatures for CO2 hydrogenation to light olefins. Applied Catalysis A: General 2017;547:219–29. https://doi.org/10.1016/j.apcata.2017.09.006.

[3] Zhao J, Bao J, Yang S, Niu Q, Xie R, Zhang Q, Chen M, Zhang P, Dai S. Exsolution–Dissolution of Supported Metals on High-Entropy Co 3 MnNiCuZnO x : Toward Sintering-Resistant Catalysis. ACS Catal 2021;11:12247–57. https://doi.org/10.1021/acscatal.1c03228.

[4] Ashok J, Ang ML, Kawi S. Enhanced activity of CO2 methanation over Ni/CeO2-ZrO2 catalysts: Influence of preparation methods. Catalysis Today 2017;281:304–11. https://doi.org/10.1016/j.cattod.2016.07.020.

[5] Dias YR, Perez-Lopez OW. Carbon dioxide methanation over Ni-Cu/SiO2 catalysts. Energy Conversion and Management 2020;203:112214. https://doi.org/10.1016/j.enconman.2019.112214.

[6] Schubert M, Pokhrel S, Thomé A, Zielasek V, Gesing TM, Roessner F, Mädler L, Bäumer M. Highly active Co–Al 2 O 3 -based catalysts for CO 2 methanation with very low platinum promotion prepared by double flame spray pyrolysis. Catal Sci Technol 2016;6:7449–60. https://doi.org/10.1039/C6CY01252C.

[7] Mutz B, Carvalho HWP, Mangold S, Kleist W, Grunwaldt J-D. Methanation of CO2: Structural response of a Ni-based catalyst under fluctuating reaction conditions unraveled

by operando spectroscopy. Journal of Catalysis 2015;327:48–53. https://doi.org/10.1016/j.jcat.2015.04.006.
[8] Xiao J, Mao D, Guo X, Yu J. Effect of TiO2, ZrO2, and TiO2–ZrO2 on the performance of CuO–ZnO catalyst for CO2 hydrogenation to methanol. Applied Surface Science 2015;338:146–53. https://doi.org/10.1016/j.apsusc.2015.02.122.
[9] Hwang JS, Jun K-W, Lee K-W. Deactivation and regeneration of Fe-K/alumina catalyst in CO2 hydrogenation. Applied Catalysis A: General 2001;208:217–22. https://doi.org/10.1016/S0926-860X(00)00701-8.
[10] Kim J-S, Lee S, Lee S-B, Choi M-J, Lee K-W. Performance of catalytic reactors for the hydrogenation of CO2 to hydrocarbons. Catalysis Today 2006;115:228–34. https://doi.org/10.1016/j.cattod.2006.02.038.
[11] Liang B, Sun T, Ma J, Duan H, Li L, Yang X, Zhang Y, Su X, Huang Y, Zhang T. Mn decorated Na/Fe catalysts for CO $_2$ hydrogenation to light olefins. Catal Sci Technol 2019;9:456–64. https://doi.org/10.1039/C8CY02275E.
[12] Poerjoto AJ, Ashok J, Dewangan N, Kawi S. The role of lattice oxygen in CO2 hydrogenation to methanol over La1-xSrxCuO catalysts. Journal of CO2 Utilization 2021;47:101498. https://doi.org/10.1016/j.jcou.2021.101498.
[13] Jiang J, Wen C, Tian Z, Wang Y, Zhai Y, Chen L, Li Y, Liu Q, Wang C, Ma L. Manganese-Promoted Fe $_3$ O $_4$ Microsphere for Efficient Conversion of CO $_2$ to Light Olefins. Ind Eng Chem Res 2020;59:2155–62. https://doi.org/10.1021/acs.iecr.9b05342.
[14] Chen H, Lin W, Zhang Z, Jie K, Mullins DR, Sang X, Yang S-Z, Jafta CJ, Bridges CA, Hu X, Unocic RR, Fu J, Zhang P, Dai S. Mechanochemical Synthesis of High Entropy Oxide Materials under Ambient Conditions: Dispersion of Catalysts via Entropy Maximization. ACS Materials Lett 2019;1:83–8. https://doi.org/10.1021/acsmaterialslett.9b00064.
[15] Rajkumar T, Sápi A, Ábel M, Farkas F, Gómez-Pérez JF, Kukovecz Á, Kónya Z. Ni–Zn–Al-Based Oxide/Spinel Nanostructures for High Performance, Methane-Selective CO2 Hydrogenation Reactions. Catal Lett 2020;150:1527–36. https://doi.org/10.1007/s10562-019-03051-8.
[16] Choi YH, Ra EC, Kim EH, Kim KY, Jang YJ, Kang K, Choi SH, Jang J, Lee JS. Sodium-Containing Spinel Zinc Ferrite as a Catalyst Precursor for the Selective Synthesis of Liquid Hydrocarbon Fuels. ChemSusChem 2017;10:4764–70. https://doi.org/10.1002/cssc.201701437.
[17] Kierzkowska-Pawlak H, Tracz P, Redzynia W, Tyczkowski J. Plasma deposited novel nanocatalysts for CO 2 hydrogenation to methane. Journal of CO2 Utilization 2017;17:312–9. https://doi.org/10.1016/j.jcou.2016.12.013.
[18] Conrad F, Massue C, Kühl S, Kunkes E, Girgsdies F, Kasatkin I, Zhang B, Friedrich M, Luo Y, Armbrüster M, Patzke GR, Behrens M. Microwave-hydrothermal synthesis and characterization of nanostructured copper substituted ZnM2O4 (M = Al, Ga) spinels as precursors for thermally stable Cu catalysts. Nanoscale 2012;4:2018. https://doi.org/10.1039/c2nr11804a.
[19] Han B, Li Q, Jiang X, Guo Y, Jiang Q, Su Y, Li L, Qiao B. Switchable Tuning CO $_2$ Hydrogenation Selectivity by Encapsulation of the Rh Nanoparticles While Exposing Single Atoms. Small 2022;18:2204490. https://doi.org/10.1002/smll.202204490.
[20] Cui X, Gao P, Li S, Yang C, Liu Z, Wang H, Zhong L, Sun Y. Selective Production of Aromatics Directly from Carbon Dioxide Hydrogenation. ACS Catal 2019;9:3866–76. https://doi.org/10.1021/acscatal.9b00640.
[21] Morgan DJ. XPS insights: Asymmetric peak shapes in XPS. Surface & Interface Analysis 2023;55:567–71. https://doi.org/10.1002/sia.7215.

[22] McIntyre NS, Cook MG. X-ray photoelectron studies on some oxides and hydroxides of cobalt, nickel, and copper. Anal Chem 1975;47:2208–13. https://doi.org/10.1021/ac60363a034.
[23] Biesinger MC, Payne BP, Grosvenor AP, Lau LWM, Gerson AR, Smart RStC. Resolving surface chemical states in XPS analysis of first row transition metals, oxides and hydroxides: Cr, Mn, Fe, Co and Ni. Applied Surface Science 2011;257:2717–30. https://doi.org/10.1016/j.apsusc.2010.10.051.
[24] Bazylewski P, Boukhvalov DW, Kukharenko AI, Kurmaev EZ, Hunt A, Moewes A, Lee YH, Cholakh SO, Chang GS. The characterization of Co-nanoparticles supported on graphene. RSC Adv 2015;5:75600–6. https://doi.org/10.1039/C5RA12893E.
[25] Bagus PS, Nelin CJ, Brundle CRichard, Crist BV, Ilton ES, Lahiri N, Rosso KM. Main and Satellite Features in the Ni 2p XPS of NiO. Inorg Chem 2022;61:18077–94. https://doi.org/10.1021/acs.inorgchem.2c02549.
[26] Burns RG. Crystal field effects in chromium and its partitioning in the mantle. Geochimica et Cosmochimica Acta 1975;39:857–64. https://doi.org/10.1016/0016-7037(75)90031-9.
[27] Luo J-W, Song J-D, Jia W-Z, Pu Z-Y, Lu J-Q, Luo M-F. Catalytic dehydrofluorination of 1,1,1,3,3-pentafluoropropane to 1,3,3,3-tetrafluoropropene over fluorinated NiO/Cr 2 O 3 catalysts. Applied Surface Science 2018;433:904–13. https://doi.org/10.1016/j.apsusc.2017.10.102.
[28] Figgis BN, Hitchman MA. Ligand field theory and its applications. New York: Wiley-VCH; 2000.
[29] Zhou L, Shinde A, Montoya JH, Singh A, Gul S, Yano J, Ye Y, Crumlin EJ, Richter MH, Cooper JK, Stein HS, Haber JA, Persson KA, Gregoire JM. Rutile Alloys in the Mn–Sb–O System Stabilize Mn^{3+} To Enable Oxygen Evolution in Strong Acid. ACS Catal 2018;8:10938–48. https://doi.org/10.1021/acscatal.8b02689.
[30] Langell MA, Hutchings CW, Carson GA, Nassir MH. High resolution electron energy loss spectroscopy of MnO(100) and oxidized MnO(100). Journal of Vacuum Science & Technology A: Vacuum, Surfaces, and Films 1996;14:1656–61. https://doi.org/10.1116/1.580314.
[31] Nesbitt HW, Banerjee D. Interpretation of XPS Mn(2p) spectra of Mn oxyhydroxides and constraints on the mechanism of MnO_2 precipitation. American Mineralogist 1998;83:305–15. https://doi.org/10.2138/am-1998-3-414.
[32] Moulder JF, Chastain J, editors. Handbook of X-ray photoelectron spectroscopy: a reference book of standard spectra for identification and interpretation of XPS data. Update. Eden Prairie, Minn: Perkin-Elmer Corporation; 1992.
[33] Esmaeilzaei A, Vahdati Khaki J, Sajjadi SA, Mollazadeh S. Synthesis and crystallization of (Co, Cr, Fe, Mn, Ni)3O4 high entropy oxide: The role of fuel and fuel-to-oxidizer ratio. Journal of Solid State Chemistry 2023;321:123912. https://doi.org/10.1016/j.jssc.2023.123912.
[34] Shabanova IN, Trapeznikov VA. A study of the electronic structure of Fe3C, Fe3Al and Fe3Si by x-ray photoelectron spectroscopy. Journal of Electron Spectroscopy and Related Phenomena 1975;6:297–307. https://doi.org/10.1016/0368-2048(75)80039-9.
[35] Ye D, Gao S, Jiang Z, Wang X, Wang Y, Liu H, Wang H. Revealing insights into the correlations between structure and performance of CrO monometallic oxide for Hg0 capture. Journal of the Energy Institute 2023;107:101185. https://doi.org/10.1016/j.joei.2023.101185.
[36] Hoang DL, Lieske H. Temperature-programmed reduction study of chromium oxide supported on zirconia and lanthana–zirconia. Thermochimica Acta 2000;345:93–9. https://doi.org/10.1016/s0040-6031(99)00385-8.

[37] Bayraktar O. Temperature-programmed reduction of metal-contaminated fluid catalytic cracking (FCC) catalysts. Applied Catalysis A: General 2004;260:125–32. https://doi.org/10.1016/j.apcata.2003.10.013.
[38] Janković B, Adnađević B, Mentus S. The kinetic study of temperature-programmed reduction of nickel oxide in hydrogen atmosphere. Chemical Engineering Science 2008;63:567–75. https://doi.org/10.1016/j.ces.2007.09.043.
[39] Steen EV, Sewell GS, Makhothe RA, Micklethwaite C, Manstein H, De Lange M, O'Connor CT. TPR Study on the Preparation of Impregnated Co/SiO2Catalysts. Journal of Catalysis 1996;162:220–9. https://doi.org/10.1006/jcat.1996.0279.
[40] Rabee AIM, Gaid CBA, Mekhemer GAH, Zaki MI. Combined TPR, XRD, and FTIR studies on the reduction behavior of Co3O4. Materials Chemistry and Physics 2022;289:126367. https://doi.org/10.1016/j.matchemphys.2022.126367.
[41] Bulavchenko OA, Gerasimov EvgenyY, Afonasenko TN. Reduction of double manganese–cobalt oxides: *in situ* XRD and TPR study. Dalton Trans 2018;47:17153–9. https://doi.org/10.1039/c8dt04137g.
[42] Ye D, Wang X, Wang R, Hu Y, Liu X, Liu H, Wang H. Relationship between Hg0 capture performance and physicochemical properties of CeO2-CrO mixed oxides. Journal of Environmental Chemical Engineering 2022;10:108252. https://doi.org/10.1016/j.jece.2022.108252.
[43] Tiernan MichaelJ, Barnes PhilipA, Parkes GarethMB. Reduction of Iron Oxide Catalysts: The Investigation of Kinetic Parameters Using Rate Perturbation and Linear Heating Thermoanalytical Techniques. J Phys Chem B 2001;105:220–8. https://doi.org/10.1021/jp003189+.
[44] Heidebrecht P, Galvita V, Sundmacher K. An alternative method for parameter identification from temperature programmed reduction (TPR) data. Chemical Engineering Science 2008;63:4776–88. https://doi.org/10.1016/j.ces.2007.10.012.
[45] Jin Y, Datye AK. Phase Transformations in Iron Fischer–Tropsch Catalysts during Temperature-Programmed Reduction. Journal of Catalysis 2000;196:8–17. https://doi.org/10.1006/jcat.2000.3024.
[46] Xu J, Zhang T, Sun Y, Fang S, Wu Z, Zhu J, Dai L, Liu W, Zhang B, Zhang J, Yao S, Gao E, Li J. Insight into the roles of superoxide-type (Mn(-O-)2Mn), bridge-type (Mn-O-Mn), and terminal-type (Mn O) oxygen species on MnO2 of different crystal structures in CO oxidation using operando TPR-DRIFTS-MS. Applied Catalysis A: General 2024;670:119519. https://doi.org/10.1016/j.apcata.2023.119519.
[47] Morales M, Barbero B, Cadus L. Total oxidation of ethanol and propane over Mn-Cu mixed oxide catalysts. Applied Catalysis B: Environmental 2006;67:229–36. https://doi.org/10.1016/j.apcatb.2006.05.006.
[48] Morales MR, Barbero BP, Cadús LE. Evaluation and characterization of Mn–Cu mixed oxide catalysts for ethanol total oxidation: Influence of copper content. Fuel 2008;87:1177–86. https://doi.org/10.1016/j.fuel.2007.07.015.
[49] Du J, Qu Z, Dong C, Song L, Qin Y, Huang N. Low-temperature abatement of toluene over Mn-Ce oxides catalysts synthesized by a modified hydrothermal approach. Applied Surface Science 2018;433:1025–35. https://doi.org/10.1016/j.apsusc.2017.10.116.
[50] Chen H, Wang Y, Lv Y-K. Catalytic oxidation of NO over MnO_2 with different crystal structures. RSC Adv 2016;6:54032–40. https://doi.org/10.1039/c6ra10103h.
[51] Zhang X, Lv X, Bi F, Lu G, Wang Y. Highly efficient Mn2O3 catalysts derived from Mn-MOFs for toluene oxidation: The influence of MOFs precursors. Molecular Catalysis 2020;482:110701. https://doi.org/10.1016/j.mcat.2019.110701.

[52] Ferrandon M, Carnö J, Järås S, Björnbom E. Total oxidation catalysts based on manganese or copper oxides and platinum or palladium I: Characterisation. Applied Catalysis A: General 1999;180:141–51. https://doi.org/10.1016/s0926-860x(98)00326-3.